Production cross sections of cosmic antiprotons in the light of new data from NA61 and LHCb experiments

(Article begins on next page)

15 July 2024

Production cross sections of cosmic antiprotons in the light of new data from the NA61 and LHCb experiments

Michael Korsmeier,[1, 2, 3, *] Fiorenza Donato,[1, 2, †] and Mattia Di Mauro[4, ‡]

[1]*Dipartimento di Fisica, Università di Torino, via P. Giuria 1, 10125 Torino, Italy*
[2]*Istituto Nazionale di Fisica Nucleare, Sezione di Torino, Via P. Giuria 1, 10125 Torino, Italy*
[3]*Institute for Theoretical Particle Physics and Cosmology,*
RWTH Aachen University, 52056 Aachen, Germany
[4]*W.W. Hansen Experimental Physics Laboratory,*
Kavli Institute for Particle Astrophysics and Cosmology,
Department of Physics and SLAC National Accelerator Laboratory,
Stanford University, Stanford, California 94305, USA

The cosmic-ray flux of antiprotons is measured with high precision by the space-borne particle spectrometers AMS-02. Its interpretation requires a correct description of the dominant production process for antiprotons in our Galaxy, namely, the interaction of cosmic-ray proton and helium with the interstellar medium. In light of new cross section measurements by the NA61 experiment of $p + p \to \bar{p} + X$ and the first ever measurement of $p + \mathrm{He} \to \bar{p} + X$ by the LHCb experiment, we update the parametrization of proton-proton and proton-nucleon cross sections.

We find that the LHCb pHe data constrain a shape for the cross section at high energies and show for the first time how well the rescaling from the pp channel applies to a helium target. By using pp, pHe and pC data we estimate the uncertainty on the Lorentz invariant cross section for $p + \mathrm{He} \to \bar{p} + X$. We use these new cross sections to compute the source term for all the production channels, considering also nuclei heavier than He both in cosmic rays and the interstellar medium. The uncertainties on the total source term are up to $\pm 20\%$. and slightly increase below antiproton energies of 5 GeV. This uncertainty is dominated by the $p + p \to \bar{p} + X$ cross section, which translates into all channels since we derive them using the pp cross sections. The cross sections to calculate the source spectra from all relevant cosmic-ray isotopes are provided in the Supplemental Material. We finally quantify the necessity of new data on antiproton production cross sections, and pin down the kinematic parameter space which should be covered by future data.

INTRODUCTION

With the last generation of particle detectors in space, physics of charged cosmic rays (CRs) has become a precision discipline. During the last decade, the space-based spectrometers PAMELA and AMS-02, which is borne to the International Space Station, have driven measurement uncertainties in the CR fluxes as low as the percent level in an energy range from 1 GeV to a few TeV. They have measured the CR nuclear [1–5] and leptonic (positron and electron) [6–10] components, as well as CR antiprotons [11, 12]. The most recent antiproton flux measurement by AMS-02 extends from 1 to 400 GeV with an uncertainty of 5% for almost the whole energy range. The new precise flux data have stimulated various analyses on Galactic CR propagation and particle dark matter annihilation into antimatter (see, e.g., [13–16]). However, to infer correct conclusions on any modeling and interpretation, an accurate description of the underling antiproton production is necessary. It is generally established that the bulk of antiprotons in our Galaxy is produced by the interaction of CRs on the interstellar medium (ISM) [17], conventionally

called secondary antiprotons. In practice, the dominant contribution is provided by the proton-proton (pp) channel, namely CR proton on ISM hydrogen, and either the CR projectile or the ISM target replaced by helium (Hep, pHe, and HeHe). Heavier channels can contribute at the few percent level.

In a first paper [18] (hereafter DKD17), we discussed the requirement on cross section measurements to determine the antiproton source term at the uncertainty level of AMS-02 flux data. Here we invert our perspective and seek to determine the source term and its uncertainty from existing cross section measurements. In general, there are two different strategies to parametrize the energy-differential cross section which enters the source term calculation. The first possibility is to find an analytic description of the fully-differential and Lorentz invariant cross section performing a fit to cross section data. Then, a Lorentz transformation and angular integration are applied to find the energy-differential cross section. This strategy was first pursued by [19]. The other option is to use Monte Carlo predictions to extract the required cross section. This was, for example, done with DTUNUC [20, 21] and more recently using EPOS-LHC and QGSJET-II-04 by Kachelriess *et al.* [22] (hereafter KMO). These Monte Carlos, EPOS and QGSJET, were originally developed for very high-energy interactions as for example occurring in CR air showers, but a special training to low-energy data al-

arXiv:1802.03030v2 [astro-ph.HE] 4 Jun 2018

lows to apply them to Galactic CR antiprotons. However, this approach only gives robust results above an antiproton energy of 10 GeV, which is a drawback considering that AMS-02 antiproton data reach down to 1 GeV. Analytic parameterizations overcome this limit, since they are directly based on the relevant low-energy data. We pursue an analytic parametrization in the following. With respect to previous analysis [13, 16, 23], we exploit new data by the NA61 experiment [24] in the pp channel and the first ever determination of pHe data by the LHCb experiment [25].

I. STATE OF THE ART ON THE ANTIPROTON SOURCE TERM

We first shortly review the basic equations and procedure to calculate the cosmic antiproton source term. The source term q_{ij} originating from the interaction of the CR component i on the ISM component j is given by a convolution integral of the energy-differential antiproton production cross section $d\sigma_{ij}/dT_{\bar{p}}$ with the incoming CR flux ϕ_i and the ISM target density $n_{\text{ISM},j}$ over the CR kinetic energy per nucleon T_i:

$$q_{ij}(T_{\bar{p}}) = \int\limits_{T_{\text{th}}}^{\infty} dT_i \ 4\pi \, n_{\text{ISM},j} \, \phi_i(T_i) \, \frac{d\sigma_{ij}}{dT_{\bar{p}}}(T_i, T_{\bar{p}}). \quad (1)$$

Here T_{th} is the energy threshold for antiproton production and the factor 4π corresponds the angular integration of an isotropic CR flux. However, experiments do not directly measure the energy-differential cross section but rather the fully-differential cross section, usually expressed in a Lorentz invariant form

$$\sigma_{\text{inv}} = E\frac{d^3\sigma}{dp^3}(\sqrt{s}, x_{\text{R}}, p_{\text{T}}), \quad (2)$$

where E is the total antiproton energy and p its momentum. It is typically a function of the kinematic variables $\sqrt{s}$, $x_{\text{R}} = E_{\bar{p}}^*/E_{\bar{p}}^{\max *}$, p_{T}, which are the center-of-mass (CM) energy, the antiproton energy divided by the maximal antiproton energy in the CM frame, and the transverse antiproton momentum, respectively[1]. Notice that the kinematic variables always refer to the nucleon-nucleon CM frame. Sometimes it is convenient to replace x_{R} by the so-called Feynman variable $x_f = 2p_{\text{L}}^*/\sqrt{s}$ which is twice the longitudinal antiproton momentum divided by the CM energy. To obtain the energy-differential cross section in Eq. (1), the kinetic variables are transferred into the LAB frame, $i.e.$ the frame where the target particle is at rest, by means of a Lorentz transformation. Suitable variables in the LAB frame are the kinetic energies of the CR T_i and of the

antiproton $T_{\bar{p}}$, and the angle θ of the produced antiproton with respect to the incident CR. Finally, the integral over the solid angle Ω relates to the energy-differential cross sections:

$$\frac{d\sigma_{ij}}{dT_{\bar{p}}}(T, T_{\bar{p}}) = p_{\bar{p}} \int d\Omega \ \sigma_{\text{inv}}^{(ij)}(T_i, T_{\bar{p}}, \theta). \quad (3)$$

More details and explicit calculations are presented in DKD17.

The dominant channels for the production of secondary antiprotons are pp at roughly 50-60% of the total spectrum, and pHe and Hep at 10-20% each, while the channels involving heavier incoming CRs contribute only up to a few percent (see below). Until very recently, no measurements of the helium channels were available, rendering the pp channel the baseline for any scaling to proton-nucleus (pA) or nucleus-nucleus (AA) channels. Often this was done in a very simplified assumption, where each nucleon of the target interacts with each nucleon of the projectile, such that the nucleon-nucleon interaction scales according to the pp one. To first order, one expects a re-scaling of pp by a factor A^D. The value of the parameter D is typically chosen between 2/3, corresponding to an approximation in which the target area is estimated from a classical sphere, and 1, if all nucleons interact completely independently. A parameterization for the cross sections involving helium (as projectile and/or target) should be derived phenomenologically from data in this specific channel. In order to be reliable, the data should cover a wide portion of the kinematical parameter space relevant for antiproton energies of interest. As we will discuss below, the first data on pHe scattering do not fulfil this condition. Therefore, in the following of this paper we rely on re-scaling from pp cross sections, which implies that uncertainties from this channel almost directly translate into the helium and heavier channels. Given the importance of the $p + p \to \bar{p} + X$ channel, we review it below.

A. The proton-proton channel

The latest analyses of the antiproton production cross section were done by Di Mauro $et\ al.$ [23] and Kappl $et\ al.$ [13], which were both triggered by newly available precise data from the NA49 experiment [26]. NA49 measures antiprotons in a fix-target pp collision at $\sqrt{s} = 17.3$ GeV. The two analyses follow slightly different strategies. On the one hand, [23] combined the NA49 data with a series of old data sets spanning a range in CM energies from $\sqrt{s} = 6.1$ GeV to 200 GeV. They perform a global fit to extract a parametrization of the fully-differential Lorentz invariant cross section. On the other hand, [13] relies on NA49 data and exploits the scaling invariance of the cross section above $\sqrt{s} =10$ GeV, namely the fact that the cross section does not depend on $\sqrt{s}$: $\sigma_{\text{inv}}(\sqrt{s}, x_{\text{R}}, p_{\text{T}}) \approx \sigma_{\text{inv}}(x_{\text{R}}, p_{\text{T}})$. Below 10 GeV, the scaling invariance is supposed to be

---

[1] The superscript * denotes that a quantity is taken in the CM frame.

violated. The two analyses pointed out two issues not considered in previous parameterizations: isospin violation and hyperon induced production. In order to calculate the total amount of antiprotons produced in our Galaxy, one has to include all the particles which decay into antiprotons, namely antineutrons and antihyperons. Traditionally, it has been assumed that antiproton and antineutron production in pp collisions is equal, and the antiproton source term has simply been multiplied by a factor 2 to account for the contribution from antineutron decays. Indeed, NA49 data [27] indicate an enhanced production of antineutrons with respect to the antiproton one. Following [16], we consider a $\sqrt{s}$ dependent isospin violation, which is estimated not to exceed 20%. The second issue has a similar origin. A fraction of the total antiproton yield originates from an intermediate antihyperon, which subsequently decays to an antiproton. The NA49 collaboration explicitly corrects and subtracts antiprotons originating from hyperons. However, the hyperon correction in older experiments is not always clearly taken into account, and data are not easily comparable. The usual assumption is that those experiments were not able to distinguish between primary (prompt) antiprotons and intermediate hyperon states, and contain a hyperon contamination which is of the order of 30%-60%. In an update of [13], Winkler [16] discusses the energy dependence of isospin violation and hyperon production. Furthermore, he points out that the scaling invariance of the cross section is broken above $\sqrt{s} = 50$ GeV such that the p_{T}-shape and normalization of the cross section require to be adjusted. High-energy collider data are used to specify and parametrize the scaling violation. Finally, above $\sqrt{s}=10$ GeV the analytic result in [16] agrees with the Monte Carlo approach by KMO, hinting that towards high energies the descriptions become robust, which is expected since the cross sections are constrained by precise NA49 and LHC data. Below 10 GeV the situation is different, because the relevant data taken in the 70's or 80's incorporate large (systematic) uncertainties.

Very recently the NA61 experiment published antiproton cross section measurements at four different CM energies $\sqrt{s}$=7.7, 8.8, 12.3 and 17.3 GeV, corresponding to beam proton energies T_p=31, 40, 80, and 158 GeV, respectively [24]. The data are corrected for hyperons and, compared to NA49, extend to lower $\sqrt{s}$. To see how much the NA61 data improve our knowledge about the pp antiproton source term, we conduct the following exercise. We calculate the fraction of the pp source term originating from the kinematic parameter space of the cross section which is experimentally determined by NA49 and NA61, respectively. Fig. 1 shows this fraction normalized to the total pp source term, $i.e.$ integrated on the whole kinematic parameter space. In more detail, the source term in Eq. (1) contains an integral over T_p, or equivalently $\sqrt{s}$, while NA49 data are taken for one fixed value of $\sqrt{s}$. In order to extract meaningful results we have to know the cross section
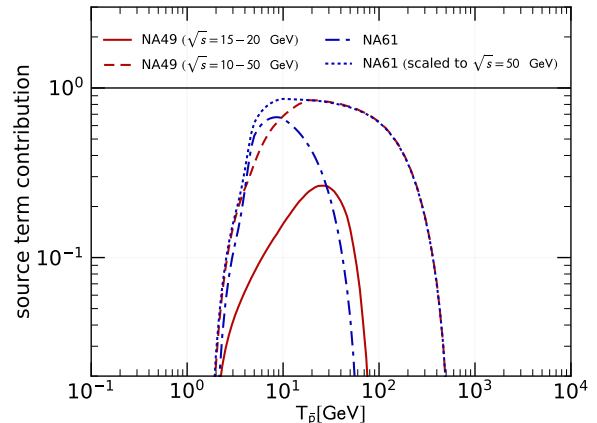

FIG. 1. Fraction of the pp source term originating from the kinematic parameter space of the cross section which is experimentally determined by NA49 and NA61. The contribution is normalized to the total pp source term. The NA61 data are taken for $\sqrt{s} = 7.7$ GeV to 17.3 GeV (blue dot-dashed line), while the NA49 is taken at $\sqrt{s} = 17.3$ GeV and here assumed to be valid in the range 15-20 GeV (solid red line). The red dashed line is obtained assuming that the NA49 data are valid in the $\sqrt{s}$ range from 10 to 50 GeV, while the dotted blue one is obtained extending the validity of NA61 data up to $\sqrt{s} = 50$ GeV. More explicitly, we assume a range from $\sqrt{s} = 7.7$ GeV to 50 GeV.

over a non-zero range in $\sqrt{s}$. A conservative assumption is that the NA49 cross section is known in a small range around 17.3 GeV, we choose $\sqrt{s} = 15$ to 20 GeV. From Fig. 1 we draw the conclusion that the experimental data of NA49 (narrow $\sqrt{s}$ range) contribute 20% to the antiproton source spectrum, peak around $T_{\bar{p}} = 30$ GeV, and quickly decrease towards smaller or larger energies. The information contained in this data gets totally negligible for $T_{\bar{p}} < 15$ GeV and $T_{\bar{p}} > 70$ GeV. In contrast to NA49, the NA61 experiment performed runs also at lower $\sqrt{s}$, which significantly improves the coverage of the contribution to the source spectrum. The experimental data of NA61 account for up to 70% and peak at $T_{\bar{p}}$ around 8 GeV. As a matter of fact, the contribution of the true experimental data to the total source spectrum covers a relatively small range in $T_{\bar{p}}$. One might wonder how this can lead to an accurate determination of the source term spectrum. The reason is the theoretical assumption of scaling invariance, according to which the cross section is independent of $\sqrt{s}$ in a range from 10 to 50 GeV [16]. In other words, we can pretend to know the cross section from $\sqrt{s} = 10$ to 50 GeV from a single measurement within the range. We therefore extend the validity of both the experiments accordingly. The results in Fig. 1 show that the NA49 parameter space can contribute between 70% and 80% from $T_{\bar{p}} \sim 10$ to 100 GeV. Above this energy, the determination of the source spectrum requires further data at large $\sqrt{s}$ de-

scribing the scaling violation. The extended NA61 data coincide with NA49 above $T_{\bar{p}} \sim 20$ GeV, while significantly improving the coverage of the source spectrum at lower energies down to 5 GeV. The baseline for our calculation in Fig. 1 is the cross section parametrization derived later in this paper (Param. II-B). However, the results are expected to be robust against changing the actual parametrization.

The conclusion of this exercise is that, in order to constrain the pp source term for $T_{\bar{p}} \lesssim 5$ GeV, it is necessary to have additional low-energy data available. Indeed, the currently available cross section measurements below $\sqrt{s} \approx 7$ GeV contain large systematic uncertainties, such that a good determination is hard to obtain. We notice that it would be useful to collect precise data at low $\sqrt{s}$ to fix the antiproton spectrum in all the energy range where CR data are now provided with an extremely high accuracy [12]. Especially, progress could be made by a $p + p \to \bar{p} + X$ experiment at energies below $\sqrt{s} = 7$ GeV. In Appendix B we show how data from NA61 at $\sqrt{s} = 6.3$ GeV could improve the cross section coverage of the pp source term. A detailed study of the complete relevant parameter space is discussed in DKD17.

B. The nuclear channels

In addition to the production of antiprotons from pp scatterings, the pHe and Hep channels contribute a large fraction of the total source term. This information may be inferred from Fig. 2, where we plot the relative contri-
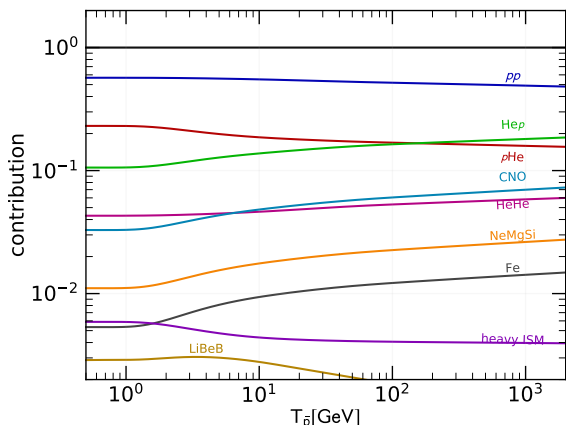

FIG. 2. Relative contribution of the various production channels to the total secondary antiproton source spectrum. The four dominant channels pp, pHe, Hep, and HeHe are given individually. We group heavy CR nuclei scattering off hydrogen and helium in the ISM: CNO, NeMgSi, Fe, and LiBeB. By heavy ISM we denote CR proton and helium scattering off the rare ISM components CNONeMgSiFe.

bution of each production channel obtained by changing the incoming CR nuclei and the ISM components. The production cross sections are taken from the results we present in Sec. III (Param. II-B). In the figure, pp, pHe, Hep, HeHe label the CR-ISM nucleus. For heavier CR nuclei, we group the reactions of LiBeB, CNO, Fe and NeMgSi CR nuclei over the ISM (p and He). We also consider the contribution from CR p and He scattering off the subdominant heavy ISM components accounted for the CNONeMgSiFe nuclei. The CR fluxes have been taken as follows: p from [3], He from [4], Li, Be and B from [28], C and O from [29], N from [30], while for all the heavier nuclei we apply the rescaling to oxygen flux as in [31]. For the ISM composition, we assume $n_{\rm H} = 1$ cm^{-3}, $n_{\rm He} = 0.1\, n_{\rm H}$, while the abundance for heavier nuclei is taken from [32]. It is clear from the figure that the channel involving He, both projectile and target, constitute 30-40% of the total spectrum depending on the antiproton energy. The heavier primary CNO nuclei contribute a non negligible few percent at the AMS energies. All the other contributions considered in this study turn out to be negligible.

Until very recently the cross sections involving He nuclei were not experimentally determined, and all calculations rely on re-scaling and extrapolation from pp and pA measurements, where A is typically carbon, but sometimes heavier nuclei up to lead. The strategy for re-scaling was either based on Monte Carlo simulations, as performed with DTUNUC at low energies [21] or KMO at high energies, or on fitting parameterizations to the scarce pA data, as performed by Duperray et al. [33]. The LHCb collaboration provides now the first ever measurement of $p + {\rm He} \to \bar{p} + X$ [25], where the incident LHC protons of 6.5 TeV momentum scatter off a fixed-target helium (corresponding to $\sqrt{s} = 110$ GeV). The LHCb detector can measure antiprotons with a momentum between 10 and 100 GeV and transverse momentum varying between 0.5 and 3.4 GeV. In [34] these data are compared to the parametirization of [16] showing reasonable agreement. Fig. 3 shows the fraction of the LHCb parameter space to the pHe and Hep source terms. We make the conservative assumption that the cross section is only known in a small (roughly 10%) range around the measured $\sqrt{s}$. In this case, the contribution to the pHe channel is at the permille level, peaking at an energy between between 10 and 100 GeV, while the contribution to the Hep channel is significantly larger at the 4% level. The different coverage of the pHe source spectrum in the inverse Hep kinematic configuration depends on the fact that in the CM frame all but one LHCb data point correspond to backwards scattering in the pHe system, or equivalently forwards scattering in the Hep system. The source term integral in Eq. (1) enhances the high-energy forward scattering due to the convolution with the steeply falling CR flux. Since in any case the contribution of the LHCb data to the source terms is very small, it is impossible to base the calculation of the $p + {\rm He} \to \bar{p} + X$ production

solely on LHCb data. In the parameterization of the pHe cross section, we will therefore rely on a re-scaling of the pp ruled by the pC data from NA49 [35], taken at $\sqrt{s} = 17.3$ GeV. Their contribution to the source term, as visible in Fig. 3, is comparable in energy and amount to the pp contribution from NA49.

The important conclusion from Fig. 3 is that the current LHCb data are not yet sufficient to give a full picture of the the antiproton production spectrum in the helium channels and its uncertainties. The contribution of the incoming p or He at the highest energy contribute only a small fraction to the produced antiprotons, in particular, referring to AMS-02 energies. This result is due to the fact that during the computation of the source spectrum the cross section is folded with an incident beam, namely the CR flux, which follows an energy power law with index of about -2.7. Nonetheless, the LHCb data contain valuable information: It shows for the first time how well the rescaling from the pp channel applies to a helium target and how the cross section extrapolation to high energies works. Moreover, finding an agreement between LHCb data and predictions based on pp and pC, increases trust in our current approaches and models. The way to improve the contribution of LHCb and the significance of its data is to increase the antiproton detection threshold above 100 GeV and/or lowering the incident proton energy below 1 TeV. In Appendix B we present predictions for the contribution with LHCb data at lower CM energies. Furthermore, we give an update of the results from DKD17 in Appendix C to determine the whole relevant parameter space of pA cross sections to interpret AMS-02 data.
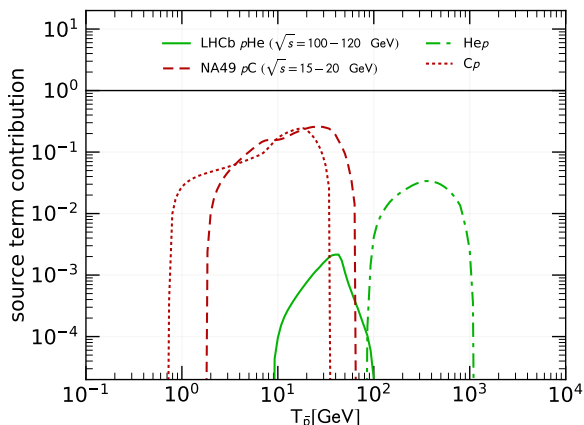

FIG. 3. Similar to Fig. 1, but for the nuclear channel. It shows the fraction of the antiproton source term which is covered by the kinematic parameter space of the cross section measurements by NA49 pC and LHCb pHe. Specifically, we assume a range of $\sqrt{s} = 15$-20 GeV for NA49 and 100-120 GeV for LHCb. Each contribution is normalized to the total source term of the specific channel.

The update takes into account the asymmetry of the cross section, namely it is given in terms of x_f instead of $x_{\rm R}$.

II. FITTING THE PROTON-PROTON CHANNEL

The proton-proton channel is relevant since it contributes about 40% of the total and, furthermore, it is the baseline for re-scaling to heavier nuclei, and for treating the contribution from antineuterons and hyperons. Its accurate determination is of central importance, since any uncertainty in pp directly translates into all the other channels. In the following we test and update the most recent analytic parametrizations by Di Mauro *et al.* [23] and Winkler [16], employing the NA49 [26] and the newly available NA61 data [24]. To reduce systematic biases we will try to discard most of the old data sets. Before turning to the fit results, we devote separate discussions to hyperons and isospin violation, the cross section parameterizations, the cross section data sets, and the fitting procedure.

A. Isospin violation and hyperons

The fits that we are going to perform are on the prompt antiproton production, so that antineutrons or antihyperons which subsequently decay into antiprotons are excluded from the fit. The estimate of the antiproton source term in the Galaxy requires the addition of these contributions by re-scaling from the prompt production

$$\sigma_{\rm inv}^{\rm Galaxy} = \sigma_{\rm inv}(2 + \Delta_{\rm IS} + 2\Delta_\Lambda), \qquad (4)$$

where $\Delta_{\rm IS}$ is the enhancement factor of antineutron with respect to antiproton production and Δ_Λ is the hyperon factor[2]. The investigations in [16] indicate that the factors $\Delta_{\rm IS}$ and Δ_Λ are energy dependent. We adopt these results and shortly repeat the analytic formulas for completeness:

$$\Delta_{\rm IS} = \frac{c_1^{\rm IS}}{1 + (s/c_2^{\rm IS})^{c_3^{\rm IS}}}, \qquad (5)$$

with $c_1^{\rm IS} = 0.114$, $c_2^{\rm IS} = (144\,{\rm GeV})^2$, and $c_3^{\rm IS} = 0.51$ and

$$\Delta_\Lambda = 0.81\left(c_1^\Lambda + \frac{c_2^\Lambda}{1 + (c_3^\Lambda/s)^{c_4^\Lambda}}\right), \qquad (6)$$

with $c_1^\Lambda = 0.31$, $c_2^\Lambda = 0.30$, $c_3^\Lambda = (146\,{\rm GeV})^2$, and $c_4^\Lambda = 0.9$. The uncertainties of these parameters have been determined in [16]. Their impact on the antiproton spectrum is discussed later in this paper.

―――――

[2] We assume that the antiproton and antineutron production from hyperons is equal.

B. Cross section parametrization

We use two parameterizations in the fit: Eq. (12) by Di Mauro *et al.* [23] (hereafter Param. I) and Winkler [16] (Param. II). Both formulae are given for the Lorentz invariant cross section in the CM frame as a function of the kinetic variables $\sqrt{s}$, x_R, and p_T. Param. I depends on 8 fit parameters $\mathcal{C} = \{C_1...C_8\}$

$$\sigma_{\mathrm{inv}}(\sqrt{s}, x_R, p_T) = \sigma_{\mathrm{in}}(1 - x_R)^{C_1} \exp(-C_2 x_R) \quad (7)$$
$$\times \left[C_3 \left(\sqrt{s}\right)^{C_4} \exp(-C_5 p_T) \right.$$
$$\left. + C_6 \left(\sqrt{s}\right)^{C_7} \exp\left(-C_8 p_T^2\right) \right].$$

The pre-factor σ_{in} is the total inelastic pp cross section and its energy-dependent form is given in [23] (Appendix B). We note that this parametrization allows freedom for the scaling with $\sqrt{s}$ and p_T. Especially, it includes an increasing normalization $\sigma_{\mathrm{in}}(s)$ which is determined by a separate fit to data.

Param. II depends only on 6 parameters $\mathcal{C} = \{C_1...C_6\}$ and is given by

$$\sigma_{\mathrm{inv}}(\sqrt{s}, x_R, p_T) = \sigma_{\mathrm{in}} R \, C_1 (1 - x_R)^{C_2} \quad (8)$$
$$\times \left[1 + \frac{X}{\mathrm{GeV}}(m_T - m_p) \right]^{\frac{-1}{C_3 X}},$$

where $m_T = \sqrt{p_T^2 + m_p^2}$. The factor

$$R = \begin{cases} 1 & \sqrt{s} \geq 10\,\mathrm{GeV} \\ \left[1 + C_5 \left(10 - \frac{\sqrt{s}}{\mathrm{GeV}} \right)^5 \right] & \text{elsewhere} \\ \times \exp\left[C_6 \left(10 - \frac{\sqrt{s}}{\mathrm{GeV}} \right)^2 \right. \\ \left. \times (x_R - x_{R,\mathrm{min}})^2 \right] \end{cases} \quad (9)$$

describes the scaling violation of the cross section at low $\sqrt{s}$, and $x_{R,\mathrm{min}} = m_p / E_{\bar{p}}^{\mathrm{max}*}$. As before, σ_{in} is the total inelastic CR cross section, whose form is determined to be

$$\sigma_{\mathrm{in}} = c_{\mathrm{in},1} + c_{\mathrm{in},2} \log\left(\sqrt{s}\right) + c_{\mathrm{in},3} \log^2\left(\sqrt{s}\right), \quad (10)$$

with $c_{\mathrm{in},1} = 30.9$ mb, $c_{\mathrm{in},2} = -1.74$ mb, and $c_{\mathrm{in},3} = 0.71$ mb. Finally, the last factor of Eq. (8) describes the scaling violations at large $\sqrt{s}$. This factor contains the parameter

$$X = C_4 \log^2\left(\frac{\sqrt{s}}{4m_p}\right). \quad (11)$$

The scaling violation at large energies affects the cross section parametrization in two ways. Firstly, the total inelastic pp cross section rises according to Eq. (10) and, secondly, the p_T shape is changed as described by the last factor of Eq. (8). Scaling violations were intensively studied in by Winkler [16] and found not to affect the behavior of the cross section below $\sqrt{s} = 50$ GeV. In this analysis we are interested in low-energy part, where NA61 adds new data. A closer look at Eq. (8) reveals

TABLE I. Summary of all pp data sets, their available CM energies, and references. Moreover, we declare which parametirzation (I or II) is used and which scale uncertainty σ_{scale} is adopted in the fits (see Eq. (14)).

Experiment	$\sqrt{s}$ [GeV]	σ_{scale}	I	II	Ref.
NA49	17.3	6.5%	×	×	[26]
NA61	7.7, 8.8, 12.3, 17.3	5%	×	×	[24]
Dekkers *et al.*	6.1, 6.7	10%	×	×	[36]
BRAHMS	200	10%	×		[38]

that the parameter C_3 determines the p_T shape at low energies, while C_4 regulates the strength of alteration towards high energies. So, we fix the parameter $C_4 = 0.038$ [16], while allowing the other 5 parameters to vary freely.

C. Data

The main data sets to constrain the fit on $\sigma_{p+p \to \bar{p}+X}$ are the NA49 [26] and NA61 [24] ones. However, the discussion about Fig. 1 revealed the necessity of a further data set at low energies to fix the antiproton source term below $T_{\bar{p}} = 5$ GeV. There are only two available data sets at these energies: Dekkers *et al.* [36] taken at $\sqrt{s} = 6.1$ and 6.7 GeV and Allaby *et al.* [37] at $\sqrt{s} = 6.15$ GeV. We use the measurements by Dekkers *et al.* , while the data set by Allaby *et al.* [37] is not taken into account because it contains very small statistical errors in combination with large systematic and normalization uncertainties. When fitting Param. I, we add data from the BRAHMS experiment, which is taken in pp collisions at $\sqrt{s} = 200$ GeV [38], in order to fix the freedom of the high-energy behavior in this parameterization. In the case of Param. II, we fixed the high-energy behavior (see discussion above) and, thus, the additional data set is not necessary. A summary of all pp data is given in Table I. The NA49 and NA61 collaborations explicitly determine the prompt antiproton flux, namely, hyperon-induced antiprotons are subtracted from the original data. However, for older experiments the situation is not completely clear. Since hyperons have a very short life-time, they usually decay inside the detector and can contribute to the measurement. Modern detectors, such as NA49, NA61 and LHCb, can reconstruct a primary vertex and discard hyperon-induced antiprotons. The usual assumption for older experiments is that they did not distinguish between hyperon-induced and prompt antiprotons. Thus, to use their data, in our case Dekkers *et al.* and BRAHMS, we subtract the hyperon contribution according to Eq. (6). Since antineutrons have a far longer lifetime compared to hyperons, they never decay inside the detector and do not require a similar correction.

D. Fit Procedure

We perform a χ^2-fit using the MINUIT package from ROOT[3] software framework in order to minimize the χ^2, which is divided into two terms:

$$\chi^2(\mathcal{C},\omega) = \chi^2_{\text{stat}}(\mathcal{C},\omega) + \chi^2_{\text{scale}}(\omega). \qquad (12)$$

The first term accounts the statistical information and contains a sum over all the data points i_k of all the experiments k from 1 to L:

$$\chi^2_{\text{stat}}(\mathcal{C},\omega) = \sum_{k=1}^{L} \sum_{i_k} \frac{\left(\omega_k \sigma_{\text{inv},i_k} - \sigma_{\text{inv}}(\mathcal{C},\mathcal{T})_{,i_k}\right)^2}{\omega_k^2 \sigma_{i_k}^2}. \quad (13)$$

Here σ_{inv,i_k} is the i_k data point for invariant cross section having total uncertainty σ_{i_k}, which is taken as the quadratic sum of statistical and systematical uncertainties of each data point if both are stated separately. The cross section parametrization $\sigma_{\text{inv}}(\mathcal{C},\mathcal{T})$ is evaluated (either for Param. I or II) at the parameter set $\mathcal{C}$ and the kinematic variables $\mathcal{T} = \sqrt{s}^{(i_k)}, x_{\text{R}}^{(i_k)}, p_{\text{T}}^{(i_k)}$. For each data set we allow a re-scaling by a constant factor ω_k, which penalizes the χ^2 by the second term in Eq. (12), explicitly given by

$$\chi^2_{\text{scale}}(\omega) = \sum_{k=1}^{L} \frac{(\omega_k - 1)^2}{\sigma_{\text{scale},k}^2}, \qquad (14)$$

where $\sigma_{\text{scale},k}$ is the scale uncertainty for each data set (see Table I). Note that the sum in Eq. (13) runs over every single data point, while the sum in Eq. (14) only runs over all data sets. Indeed, a scale uncertainty requires that all points are correlated. Moving up or down all the data points of each set by the same factor is only penalized once, not for each data point. This is in contrast to the treatment in [23] (although stated differently in the paper). NA49 explicitly states scale uncertainties of 6.5%. For the other experiments we estimate the scale uncertainty according to the average size of the systematic uncertainties to be 5% for NA61, and 10% for Dekkers et $al.$ and BRAHMS. During the fit we simultaneously adjust $\mathcal{C}$ and the nuisance parameters $\omega = \omega_1...\omega_L$, leaving in total 12 free parameters for Param. I and 8 for Param. II. In practice, we use the ROOT algorithms in two steps to minimize our χ^2. First, the MIGRAD algorithm determines a good parameter estimate, then the HESSE algorithm confirms these parameters and gives a more reliable covariance matrix.

E. Results

We find that both parametrizations Eq. (7) and (8), result in a good fit to the pp cross section data, giving a

---

χ^2/ndf of 1.30 and 1.18 for Param. I and Param. II, respectively. The best fit parameters with the relevant 1σ uncertainties are summarized in Table II. We present the full correlation matrix in the Appendix. Furthermore, we demonstrate in Table III that reduced χ^2s for all data sets are close to one, namely, all data sets in the fit are consistent with each other, if we allow for a re-scaling by the nuisance parameters ω_k. There seems to be a general tendency to scale down the NA61 data by 6-7%, while increasing the NA49 data by about 6% and the Dekkers data by 5-9% in both parametrizations. Especially, we note that NA49 and NA61 have an overlap in the kinetic parameter space at $\sqrt{s} = 17.3$ GeV. After the slight re-scaling the two data sets are in agreement with each other.

In Fig. 4 we report our results for the differential cross section $d\sigma/dT_{\bar{p}}(p + p \rightarrow \bar{p} + X)$ for the production of prompt antiprotons, at the representative proton energies $T_p = 20$ GeV, 450 GeV and 6.5 TeV. The uncertainty bands are derived from our fits (see discussion about Fig. 5), and go from 20% at $T_p = 20$ GeV to 10% for $T_p = 450$ GeV and 6.5 TeV. For the lower T_p value the to predictions are mildly compatible, while they almost overlap for higher energies. We also report some estimates from recent literature, showing some discrepancy with our findings mostly at low $T_{\bar{p}}$ for the Di Mauro and the Winkler parameterizations. The Monte Carlo based KMO parameterization has been divided by 2.3 since it accounts all the antiprotons produced in the interaction, $i.e.$ not only the prompt ones. We provide tables with the total (antiprotons from prompt production, from antineutron and antihyperon dacay) cross section for a full T_p scan - as well as for a number of other incoming particles on p and He - in the Supplemental Material.

We calculate the $\bar{p}$ source term from the two cross sec-

TABLE II. Fit results to the $p + p \rightarrow \bar{p} + X$ cross section. The full correlation matrices are given in Table VIII and Table IX.
(*) The parameter C_4 is fixed, $i.e.$ not included in the fit, in Param. II (see text for details).

	with Param. I	with Param. II
C_1	3.50 ± 0.64	$(5.02 \pm 0.22) \times 10^{-2}$
C_2	5.59 ± 0.85	7.790 ± 0.077
C_3	$(4.00 \pm 0.73) \times 10^{-2}$	$(1.649 \pm 0.012) \times 10^{-1}$
C_4	-0.251 ± 0.071	$(3.800 \pm 0.057) \times 10^{-2}$ (*)
C_5	2.651 ± 0.097	$(4.74 \pm 2.59) \times 10^{-4}$
C_6	$(3.78 \pm 0.53) \times 10^{-2}$	3.70 ± 0.64
C_7	$(4.3 \pm 4.3) \times 10^{-2}$	-
C_8	2.695 ± 0.047	-
ω_{BRAHMS}	1.115 ± 0.079	-
ω_{Dekkers}	1.051 ± 0.068	1.090 ± 0.090
ω_{NA49}	1.059 ± 0.039	1.061 ± 0.044
ω_{NA61}	0.936 ± 0.036	0.932 ± 0.038

TABLE III. Fit quality of the pp channel. The first row reports the global fit, while the other ones show the contribution of the single data sets to the χ^2.

	with Param. I	with Param. II
χ^2/ndf	534.7/411	464.7/394
χ^2_{BRAHMS} (data points)	27.6 (21)	-
$\chi^2_{\mathrm{Dekkers}}$ (data points)	9.8 (10)	8.3 (10)
χ^2_{NA49} (data points)	211.4 (143)	179.0 (143)
χ^2_{NA61} (data points)	286.0 (249)	277.4 (249)

tion parameterizations, and compare them two previous predictions. We remind again that the fit is performed to the prompt antiproton production, and consequently the source term calculated according to Eq. (1) and displayed in Fig. 5 does not include antiprotons from neutron and hyperon decay. To calculate the fit uncertainty we sample random points in the parameter space $(\mathcal{C}, \omega)$ from the full correlation matrix and verify each point against the total χ^2 from Eq. (12). Then we compute the χ^2 profile as function of the source term, separately at each energy. The uncertainty band at 1σ ($n\sigma$) is given by $\Delta\chi^2 = 1$ ($\Delta\chi^2 = n^2$). The interpretation of this 1σ region is that in 68.3% of all cases the source term falls within the band. We checked that the size of the uncertainty band grows approximately linearly with the σ-interval. Therefore, we show only the 2σ band in our plots, a different confidence level may be obtained by rescaling. An alternative useful quantity

is the envelope of the n-dimensional χ^2 distribution at 1σ level, where n is the number of free parameters in the fit (Param. I: $n = 12$, Param. II: $n = 8$). In other words, this envelope is built from the set which contains of 68.3% of the source term realizations and has the lowest χ^2 values. We show this envelope in Fig. 5 for comparison and note that it almost coincides with the 3σ band. Finally, we obtain an uncertainty - solely from the cross section fit - of $\pm 8\%$. With Param. II it increases to about $\pm 15\%$ below 5 GeV. The source terms from Param. I and Param. II are consistent within the fit uncertainties. In particular, from $T_{\bar{p}} = 1$ GeV to a few hundred GeV, the agreement between the two models is very good. Above 500 GeV, Param. II provides an antiproton spectrum systematically higher than Param. I. In [23], it was already pointed out that Param. I - due to the employed data sets - gives reliable results up to a few hundred GeV. Param. II, which employs differ-
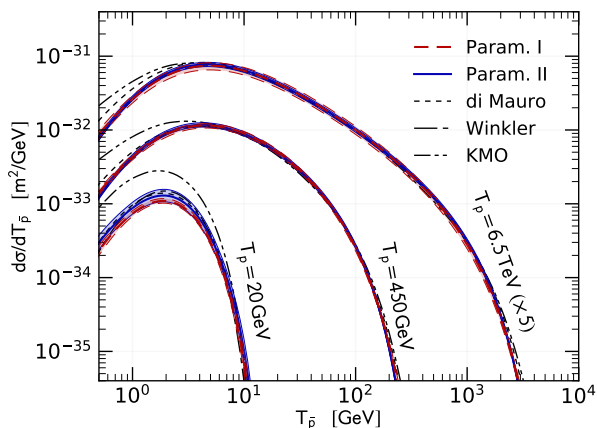

FIG. 4. The differential cross section $d\sigma/dT_{\bar{p}}(p + p \rightarrow \bar{p} + X)$ for prompt antiprotons, at the representative proton energies $T_p = 20$ GeV, 450 GeV and 6.5 TeV. The dashed (solid) line and the red (blue) band are the result of our analysis for Param. I and Param. II. The uncertainty band corresponds to the 2σ confidence interval. We report for comparison some literature estimations (see text for details). Tables with the full cross section results are provided in the Supplemental Material to this paper.
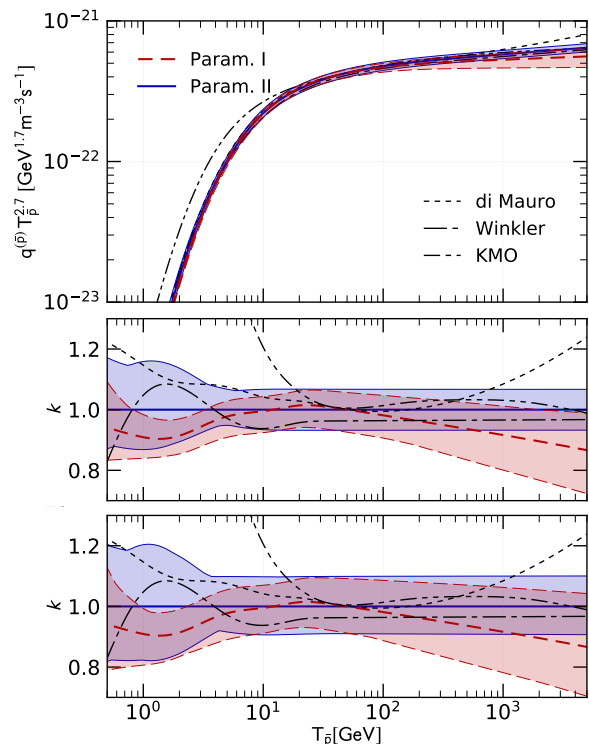

FIG. 5. Source term of prompt antiprotons originating from pp collisions and its uncertainty induced by the cross section fits of Param. I (red dashed) and Param. II (blue solid), respectively. For comparison, we show the antiproton source term from previous parametrizations Di Mauro *et al.*, Winkler and KMO. The central panel displays the ratio k to the best fit of Param. II and the shaded uncertainty bands correspond to the 2σ confidence interval. For completeness the lower panel contains the 1σ envelope of the n-dimensional χ^2 distribution (see discussion in the text for details).

ent data sets at the highest $\sqrt{s}$, is likely to give a more trustworthy result at high energies. The comparison of previous analysis by Di Mauro, Winkler and KMO reveals several interesting features. The direct (because involving the same parametrization, just different data sets) comparison between Param. I and Di Mauro shows that the source term predictions are very close between 10 and 100 GeV, while Param. I source spectrum stands systematically lower below 10 GeV and above 100 GeV. This is probably the effect of the hyperon subtraction for Dekkers and BRAHMS data, which was considered here but not in [23]. Param. II and Winkler are consistent within uncertainties. Especially, above 30 GeV the two predictions also coincide with KMO. Below 10 GeV KMO clearly deviates and overpredicts the antiproton source spectrum.

Concluding, both parametrizations for the $\sigma_{p+p\to\bar{p}+X}$ result in compatible $\bar{p}$ source terms for the energy range measured by AMS-02. The difference in the shape of the two parametrizations is only few percent in the range of $T_{\bar{p}} = 5$ to 100 GeV, however, at 1 GeV and 1 TeV it grows to 10%, where Param. I is slightly softer at high energies.

III. FITTING THE PROTON-NUCLEUS CHANNEL

The proton-nucleus channels contribute between 40 and 50% of the total secondary antiproton production. However, the currently available data on antiproton production measurement in pA collisions are not sufficient to allow an individual description of each relevant channel, especially pHe (see discussion in Sec. I). We use pC data by NA49 and pHe data by LHCb to determine a re-scaling factor for the pA and, specifically, pHe cross sections from the pp cross section.

A. Cross section parametrization

Antiproton production in pp collisions is by definition symmetric under a reflection along the beam axis in the CM frame, while this is not necessarily the case in pA collisions (in the nucleon-nucleon CM frame). Actually, NA49 pC data [35] reveals that the cross section is not symmetric between forward and backward production. It is plausible that the binding of the nucleons in the nucleus has an effect on the antiproton production and breaks the symmetry. Since a description of the cross section in terms of x_{R} which intrinsically expects symmetry is inconsistent, we will use x_f instead in the following whenever we discuss pA channels . Following the description by NA49, [13] exploits a re-scaling of pp cross section in terms of overlap functions. The idea is to split the antiproton production into two components produced by projectile and target, where the antiprotons from each component are produced mainly forward

directed. Separately adjusting the overlap functions allows to accommodate the asymmetry.   The inclusive Lorentz invariant cross section of $p + A \to \bar{p} + X$ scattering is given by

$$\sigma_{\mathrm{inv}}^{pA}(\sqrt{s}, x_f, p_{\mathrm{T}}) = f^{pA}(A, x_f, \mathcal{D})\ \sigma_{\mathrm{inv}}^{pp}(\sqrt{s}, x_{\mathrm{R}}, p_{\mathrm{T}}),(15)$$

where A is the mass number of the nucleus and $\mathcal{D} = (D_1, D_2)$ are the two fit parameters. Explicitly, the factor f^{pA} is defined by:

$$f^{pA} = A^{D_1} \left[A^{D_2} \left(1 + \frac{N}{A}\Delta_{\mathrm{IS}} \right) F_{\mathrm{pro}}(x_f) \right.$$
$$\left. + F_{\mathrm{tar}}(x_f) \right].$$
(16)

$F_{\mathrm{pro}}(x_f)$ and $F_{\mathrm{tar}}(x_f)$ are the projectile and target overlap functions. They fulfil $F_{\mathrm{tar}}(x_f) = F_{\mathrm{pro}}(-x_f)$ and $F_{\mathrm{tar}}(x_f) + F_{\mathrm{pro}}(x_f) = 1$ and are defined in Table IV. N is the number of neutrons in the nucleus. The form factor f^{pA} is motivated by [13, 35]. Its A dependence is chosen such that in the case of $A = 1$ we retain proton-proton scattering. We remind that the kinetic variables x_f and $\sqrt{s}$ refer to the nucleon-nucleon CM frame, where proton and nucleus have the same velocity, not the same momentum. Consequently, the CM energy $\sqrt{s}$ is the colliding energy of the nucleon with the proton.

The fit procedure is analogous to the pp case discussed in the previous section. However, here the parameters $\mathcal{C}$ from Eq. (15) are fixed, in other words the pp scattering is unaltered, and only the new parameters $\mathcal{D}$ are varied in the fit. The definition of our χ^2 is equivalent to Eq. (12), when $\mathcal{C}$ is replaced by $\mathcal{D}$ and k runs over the experiments with pA data. As before we allow for nuisance parameters ω of each data set.

TABLE IV. Projectile overlap function $F_{\mathrm{pro}}(x_f)$. The definition is taken from [35].

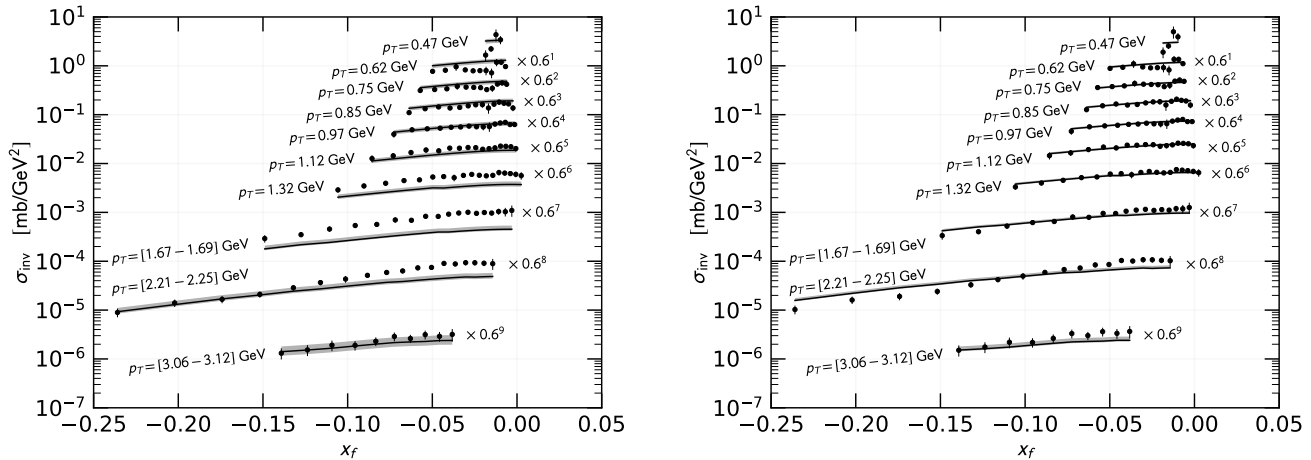| x_f	F_{pro}	x_f	F_{pro}
-0.250	0.0000	0.250	1.0000
-0.225	0.0003	0.225	0.9997
-0.200	0.0008	0.200	0.9992
-0.175	0.0027	0.175	0.9973
-0.150	0.010	0.150	0.990
-0.125	0.035	0.125	0.965
-0.100	0.110	0.100	0.890
-0.075	0.197	0.075	0.803
-0.050	0.295	0.050	0.705
-0.025	0.4	0.025	0.6
		0.000	0.5

FIG. 6. Comparison of LHCb data to the fit with Param. I-B (left) and Param. II-B (right). The grey band corresponds to 2σ uncertainty in the fit. The LHCb data agree better with Param. II and, therefore, they select this model for the high-energy behavior of the Lorentz invariant cross section.

TABLE V. Main properties of the NA49 pC and LHCb pHe data sets: available CM energies, scale uncertainty σ_{scale} adopted in the fits, the parameterization (I or II) used in the fit, references. Labels A and B refer to use of NA49 pC data alone or NA49 pC and LHCb pHe, respectively.

	$\sqrt{s}$ [GeV]	σ_{scale}	I-A	I-B	II-A	II-B	Ref.
NA49	17.3	6.5%	×	×	×	×	[35]
LHCb	110	6.0%		×		×	[25]

B. Data

We exploit the data from NA49 and LHCb on pC and pHe scattering, respectively. Both experiments use a fixed target nucleus while the incident proton is accelerated to 158 GeV in NA49 and 6.5 TeV in LHCb. Their data are very precise, and both experiments correct for antihyperons, *i.e.* they remove antiprotons originating from the decay of intermediate antihyperon states. We summarize the main experimental information in Table V.

C. Results

We perform four fits to determine, first, the goodness of the parametrizations (I and II) from the pp fit for the interpretation of nuclei data and, secondly, the impact of LHCb data by excluding (case A) or including (case B) them in the fits. Table VI comprises the results of all four fits. The fits with pC data alone (without LHCb data) I-A and II-A converge to a χ^2/ndf of 1.3 and 1.1, respectively, leaving the conclusion that the

NA49 proton-carbon data fits very well to a rescaled pp cross section. In the second step, we use the fit results to predict the pHe cross section and to compare it to LHCb data. Param. I shows a large difference between data and the prediction, measured by a χ^2/ndf from LHCb alone of 9.3. On the other hand, Param. II gives a $\chi^2/\text{ndf} = 1.6$, hinting already the good agreement with Param. II rescaled by the form factor f^{pA} fixed on pC data. Including the LHCb data in the fit does not change the general picture. The quality of the fit slightly improves to 8.4 and 1.4 in both cases I-B and II-B, respectively. We conclude that Param. II results in a much better description of the pHe data by LHCb. The best fit values for all parameters are summarized in Table VII. Our results for Param. II agree with [16] (*i.e.* $\langle \nu_{\text{He}} \rangle = 1.25$ there is comparable with $4^{D_2} = 1.22$ and $4^{1-D_1} = 1.27$). However, for pC we obtain a 10% lower value of $12^{D_2} = 1.43$ or $12^{1-D_1} = 1.53$ instead

TABLE VI. Fit quality of f^{pA} for the different pp Param. I and II, and for the different data sets A (NA49 pC) and B (NA49 pC, LHCb pHe). The first row shows the result of the fit, while the second and third rows report the split contribution from the pC NA49 and pHe LHCb data sets. In brackets are the numbers of data points entering in the fit. The italic numbers are not the result of a minimization, but the χ^2 on LHCb data with the parameters fixed by NA49 pC data.

	Param. I		Param. II	
	A	B	A	B
χ^2/ndf	153.0/118	1296.3/253	131.2/118	326.3/253
χ^2_{NA49}	153.0 (121)	155.3 (121)	131.2 (121)	131.8 (121)
χ^2_{LHCb}	*1266 (136)*	1141 (136)	*212.4 (136)*	194.5 (136)

TABLE VII. Fit results of f^{pA} for the different pp Param. I and II, and for different data sets A (NA49 pC) and B (NA49 pC, LHCb pHe).

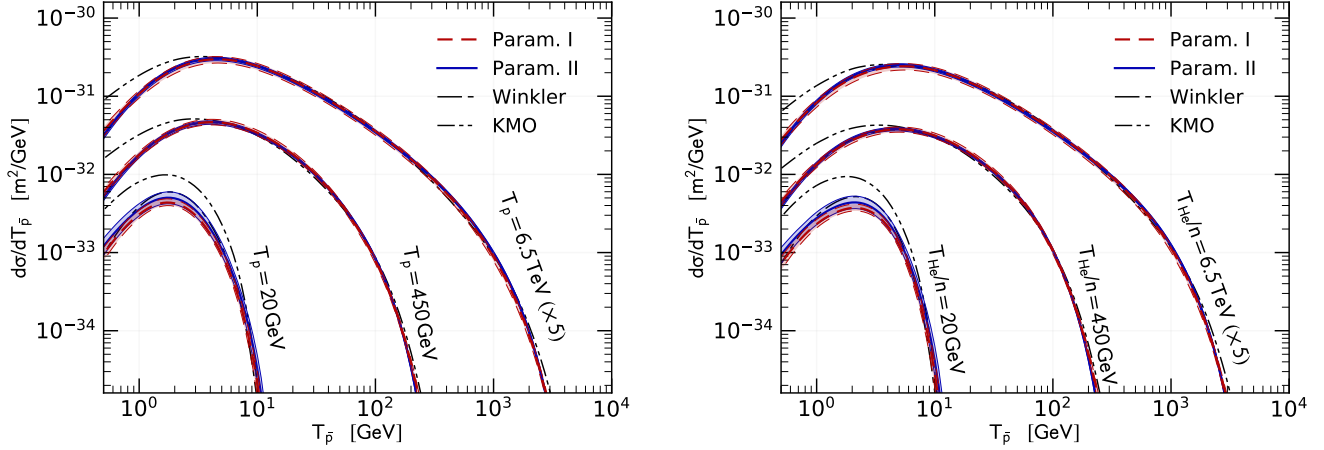|	Param. I		Param. II	
Parameter	A	B	A	B
D_1	0.830 ± 0.012	0.825 ± 0.012	0.825 ± 0.012	0.828 ± 0.012
D_2	0.149 ± 0.013	0.167 ± 0.012	0.154 ± 0.013	0.145 ± 0.012
ω_{NA49}	1.000 ± 0.025	1.001 ± 0.024	1.000 ± 0.025	0.997 ± 0.024
ω_{LHCb}	-	0.900 ± 0.015	-	1.034 ± 0.018

FIG. 7. The differential cross section $d\sigma/dT_{\bar{p}}(p + \mathrm{He} \rightarrow \bar{p} + X)$ (left) and $d\sigma/dT_{\bar{p}}(\mathrm{He} + p \rightarrow \bar{p} + X)$ (right) for prompt antiprotons, at the representative incident energies $T_p = 20$ GeV, 450 GeV and 6.5 TeV. The dashed (solid) line and the relevant red (blue) band are the result of our analysis for Param. I and Param. II. The uncertainty band corresponds to the 2σ confidence interval. We report for comparison some literature estimations (see text for details). Tables with the full cross section results are provided in the Supplemental Material to this paper.

of $\langle \nu_{\mathrm{C}} \rangle = 1.6$. Fig. 6 displays the comparison of the LHCb data to the cross section prediction. It is visible that the p_{T}-shape of Param. I does not fit well the data. This shape is inherited from the pp data, and it is therefore unlikely to improve the fit by a mere refinement of the f^{pA} parametrization. We remind that Param. II includes corrections to the p_{T}-shape due to scaling violation [16]. Finally, we remark that we explicitly tried a fit solely on LHCb data, but since the data contain, apart from one data point, only points for antiprotons produced in backward direction it cannot constrain the asymmetry imposed by D_2 and the parameters D_1 and D_2 turn out to be degenerate. To calculate $\sigma_{\mathrm{He}+p\rightarrow\bar{p}+X}$ we use a generalization of Eq. (16):

$$f^{A_1 A_2} = A_1^{D_1} A_2^{D_1} \left[A_1^{D_2} \left(1 + \frac{N_1}{A_1} \Delta_{\mathrm{IS}} \right) F_{\mathrm{pro}}(x_f) \right. \quad (17)$$
$$\left. + A_2^{D_2} \left(1 + \frac{N_2}{A_2} \Delta_{\mathrm{IS}} \right) F_{\mathrm{tar}}(x_f) \right].$$

We cross-checked the validity of this approach by taking the pHe cross section and transforming it to the frame where the proton is at rest. The two methods give the same result. Similarly to Fig. 4, in Fig. 7 we report the results for the differential cross section $d\sigma/dT_{\bar{p}}(p + \mathrm{He} \rightarrow \bar{p} + X)$ (left panel) for the representative proton energies $T_p = 20$ GeV, 450 GeV and 6.5 TeV. The right panel contains the same information but for incoming He on p. To determine the fit uncertainty we sample points from the correlation matrices of the pp and pA fits (see Appendix A). To constrain the pA fit at the 2σ confidence level we require that the total χ^2 (sum of pp and pA fit) lies within a range of $\Delta\chi^2=4$ compared to our best fit values. Additionally, we reflect the fact that the pp fit is a prior of the pA fit by requiring that also its χ^2 is within a range of $\Delta\chi^2=4$. The conclusions are similar to the pp case. We provide a full table for the total cross sections of a number of incident nuclei and their isotopes, and for both p and He fixed target in the Supplemental Material to this paper.

We use the fit results to calculate source terms for the pHe and Hep production channels. The results are shown in Fig. 8. In general, the form and uncertainty of pHe and Hep look similar to pp, since both depend on the pp parametrization. The fact that Hep is harder
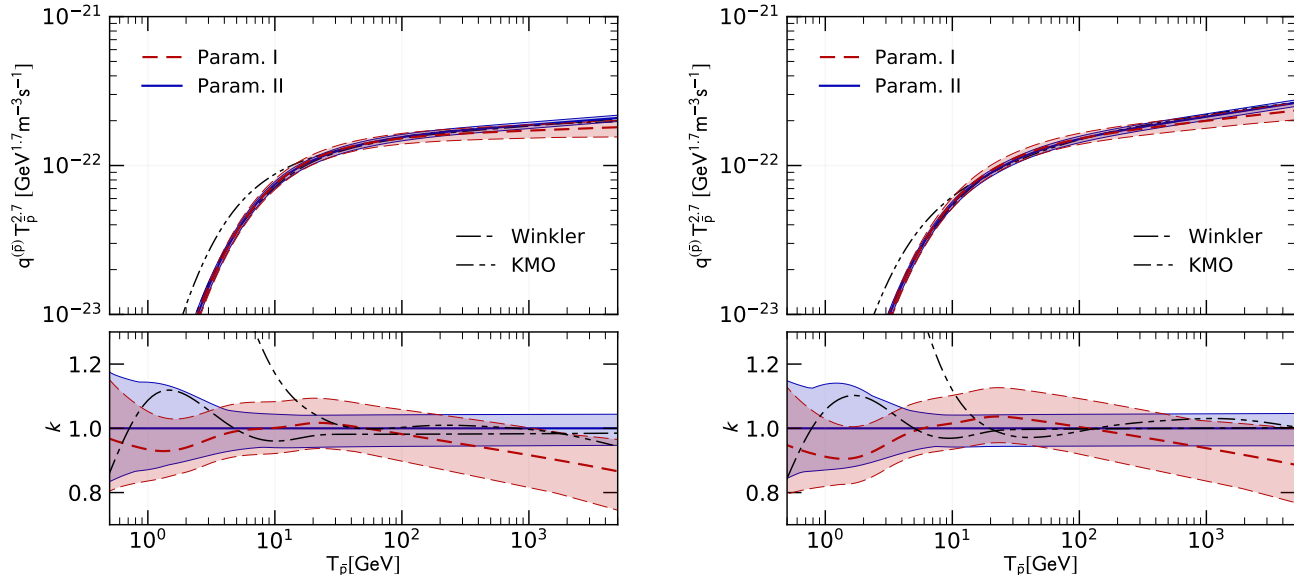
FIG. 8. CR pHe (left panel) and Hep (right panel) antiproton source term with the uncertainty on cross sections for the best fit of Param. I-B and II-B, *i.e.* with NA49 pC and LHCb pHe data. Uncertainties are given at the 2σ confidence interval.

than pHe comes from the CR flux which is harder for He compared to p. The two parameterizations are compatible within uncertainties in the AMS-02 $T_{\bar{p}}$ energy range, while Param. I implies a slightly softer $\bar{p}$ spectrum w.r.t. Param. II. The agreement with former parametrizations Winkler and KMO is unchanged compared to the pp study. However, the re-scaled Di Mauro *et al.* shows large deviation in the shape at high energies. We recommend to use the re-scaling from this paper instead.

IV. THE TOTAL ANTIPROTON SOURCE TERM

The results obtained in the previous sections can be joint to compute the total antiproton source term in the Galaxy, including antineutrons and antihyperons, and the contributions from nuclei heavier than helium. The latter, as shown in Fig. 2, give a contribution which is not negligible when compared to errors on the $\bar{p}$ flux measured by AMS-02. The CR CNO on p or He contributes to the source term at the few percent level each. Even the heavier CR primaries NeMgSi and Fe may contribute above 1%. We note that our fit is tuned to He and C data and therefore the uncertainty on cross sections is extrapolated for CR sources heavier than CNO. The total $\bar{p}$ source term is plotted in Fig. 9, along with the contribution for every production channel. We use the same inputs for CR fluxes and ISM components as discussed in the context of Fig. 2. It is visible how the measured hardening of CR nuclei fluxes with respect to

protons [4, 29] results in a corresponding hardening of the antiproton source term [39]. The rescaling from the prompt $\bar{p}$ production follows Eq. (4). We also plot the uncertainty band from the production cross sections, as determined in the fits to data on prompt antiprotons. In order to include the production from neutron and hyperon decays, we pick the parameters as declared in [16], and namely $c_1^{\text{IS}} = 0.114 \pm 0.1$ for the determination of Δ_{IS} (see Eq. (5)), and 0.81 ± 0.04, $c_1^{\Lambda} = 0.31 \pm 0.0375$, $c_2^{\Lambda} = 0.30 \pm 0.0125$ for the determination of Δ_{Λ} (see Eq. (6)).

The results in Fig. 9 show that the uncertainty due to prompt cross sections (bottom panel) is at the level of $\pm 8\%$ at 2σ above $T_{\bar{p}} = 5$ GeV. At $T_{\bar{p}} \leq 5$ GeV it increases to $\pm 15\%$ at 1 GeV. Adding the uncertainties from isospin violation in the antineutron production and from hyperon decays, the uncertainty on the total antiproton source term ranges $\pm 12\%$ from high energies down to about few GeV, and increases to $\pm 20\%$ below that value. Above $T_{\bar{p}} = 50$ GeV the total antiproton source spectrum can be approximated by a power law with an index of about -2.5 .

V. CONCLUSIONS

The role of high-energy particle physics in the interpretation of CR data receives increasing attention, since data from space are provided with improving precision. AMS-02 on the International Space Station collected data of CR nuclei, leptons, and antiprotons with un-

precedented accuracy, often pushing uncertainties down to few percent in a large range of energy from the GeV to the TeV scale. The fluxes of secondary CRs, which are produced in interactions with the ISM, depend on the inclusive production cross sections provided by high-energy particle experiments. In particular, this applies to CR antiprotons whose origin is believed to be dominantly secondary. Consequently, the interpretation of the antiproton flux in terms of CR propagation or the search for a possible primary component, such as for example dark matter annihilation or decay, relies on the accurate modeling of secondary production. The underlying cross sections should be provided at least at the same accuracy level as CR measurements.

In this paper, we analyze the first-ever data on the inclusive cross section $p + \text{He} \rightarrow \bar{p} + X$ collected by the LHCb collaboration at Cern, with beam protons at $T_p = 6.5$ TeV and a fixed helium target. Since the coverage of the kinematic parameter space of this data do not allow a standalone parametrization, we apply a rescaling from $p + p \rightarrow \bar{p} + X$ cross section. Therefore, we update the most recent parametrizations from Di Mauro *et al.* (Param. I) and Winkler (Param. II) exploiting the newly available NA61 data. Then we determine the rescaling factor to proton-nucleus using

pHe data from LHCb and pC data from NA49 (taken at $\sqrt{s} = 110$ and 17.3 GeV, respectively). The LHCb pHe data clearly prefer Param. II. All other data result in equally good fits for both parametrizations. Moreover, the LHCb data show for the first time how well the rescaling from the pp channel applies to helium target. By using pp, pHe and pC data we estimate the uncertainty on the Lorentz invariant cross section for $p + \text{He} \rightarrow \bar{p} + X$. This uncertainty is dominated by $p + p \rightarrow \bar{p} + X$ cross section, which translates into all channels since we derive them using the pp cross sections.

Finally, we use our cross sections to compute the antiproton source terms and their uncertainties for all the production channels, considering also nuclei heavier than He both in CRs and the ISM. At intermediate energies from $T_{\bar{p}} = 5$ GeV up to a few hundred GeV the prompt source terms derived from Param. I and II are compatible within uncertainties, which are at the level of $\pm 8\%$ at the 2σ level and increase to $\pm 15\%$ below $T_{\bar{p}} = 5$ GeV. The uncertainty is dominated by $p + p \rightarrow \bar{p} + X$ cross section, which translates into all channels. Antineutron- and hyperon-induced production increases the uncertainty by an additional 5%. Overall the secondary antiproton source spectrum is affected by an uncertainty of up to $\pm 20\%$. Moreover, we find that CR CNO makes up to few percent of the total source term and should always be considered. In the Supplemental Material to this paper, we provide the energy-differential cross sections, which are required to calculate the source spectrum, for all relevant isotopes. We quantify the necessity of new data on antiproton production cross sections, and pin down the kinematic parameter space which should be covered by future data.
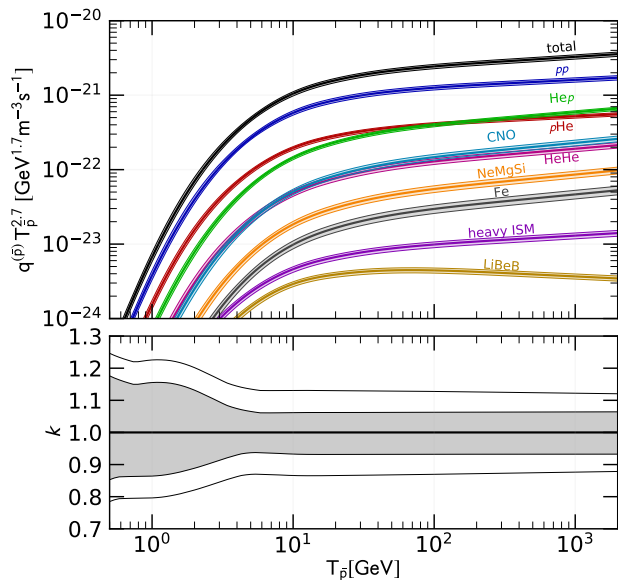

FIG. 9. Source terms of CR antiprotons and separate CR-ISM contributions, grouped following the prescriptions in Fig. 2. The shaded bands report the 2σ uncertainty due to prompt $\bar{p}$ production cross sections as derived in this paper. In the bottom panel we show the relative uncertainty on the total source term. The grey band refers to the prompt $\bar{p}$'s only, while the outer lines quantify the additional uncertainty due to isospin violation and to hyperon decay.

VI. ACKNOWLEDGMENTS

[1] O. Adriani et al. (PAMELA), Science **332**, 69 (2011), arXiv:1103.4055 [astro-ph.HE].
[2] O. Adriani et al., Astrophys. J. **791**, 93 (2014), arXiv:1407.1657 [astro-ph.HE].
[3] M. Aguilar et al. (AMS), Phys. Rev. Lett. **114**, 171103 (2015).
[4] M. Aguilar et al. (AMS), Phys. Rev. Lett. **115**, 211101 (2015).
[5] M. Aguilar et al. (AMS), Phys. Rev. Lett. **117**, 231102 (2016).
[6] O. Adriani et al., Nature (London) **458**, 607 (2009), arXiv:0810.4995.
[7] O. Adriani et al., Phys. Rev. Lett. **106**, 201101 (2011), arXiv:1103.2880 [astro-ph.HE].
[8] M. Aguilar, G. Alberti, B. Alpat, A. Alvino, G. Ambrosi, K. Andeen, H. Anderhub, L. Arruda, P. Azzarello, A. Bachlechner, and et al., Phys. Rev. Lett. **110**, 141102 (2013).
[9] M. Aguilar, D. Aisa, A. Alvino, G. Ambrosi, K. Andeen, L. Arruda, N. Attig, P. Azzarello, A. Bachlechner, F. Barao, and et al., Phys. Rev. Lett. **113**, 121102 (2014).
[10] M. Aguilar, D. Aisa, B. Alpat, A. Alvino, G. Ambrosi, K. Andeen, L. Arruda, N. Attig, P. Azzarello, A. Bachlechner, and et al., Phys. Rev. Lett. **113**, 221102 (2014).
[11] O. Adriani et al., Phys. Rev. Lett. **105**, 121101 (2010), arXiv:1007.0821 [astro-ph.HE].
[12] M. Aguilar et al. (AMS), Phys. Rev. Lett. **117**, 091103 (2016).
[13] R. Kappl and M. W. Winkler, JCAP **1409**, 051 (2014), arXiv:1408.0299 [hep-ph].
[14] M. Korsmeier and A. Cuoco, Phys. Rev. D **94**, 123019 (2016), arXiv:1607.06093 [astro-ph.HE].
[15] A. Cuoco, J. Heisig, M. Korsmeier, and M. Krmer, JCAP **1710**, 053 (2017), arXiv:1704.08258 [astro-ph.HE].
[16] M. W. Winkler, JCAP **1702**, 048 (2017), arXiv:1701.04866 [hep-ph].
[17] F. Donato, D. Maurin, P. Brun, T. Delahaye, and P. Salati, Phys. Rev. Lett. **102**, 071301 (2009), arXiv:0810.5292 [astro-ph].
[18] F. Donato, M. Korsmeier, and M. Di Mauro, Phys. Rev. **D96**, 043007 (2017), arXiv:1704.03663 [astro-ph.HE].
[19] L. C. Tan and L. K. Ng, J. Phys. **G9**, 227 (1983).
[20] M. Simon, A. Molnar, and S. Roesler, Astrophys. J. **499**, 250 (1998).
[21] F. Donato, D. Maurin, P. Salati, A. Barrau, G. Boudoul, and R. Taillet, Astrophys. J. **563**, 172 (2001), arXiv:astro-ph/0103150 [astro-ph].
[22] M. Kachelriess, I. V. Moskalenko, and S. S. Ostapchenko, Astrophys. J. **803**, 54 (2015), arXiv:1502.04158 [astro-ph.HE].
[23] M. di Mauro, F. Donato, A. Goudelis, and P. D. Serpico, Phys. Rev. **D90**, 085017 (2014), arXiv:1408.0288 [hep-ph].
[24] A. Aduszkiewicz et al. (NA61/SHINE), Eur. Phys. J. **C77**, 671 (2017), arXiv:1705.02467 [nucl-ex].
[25] G. Graziani et al. (LHCb), in 52nd Rencontres de Moriond (2017).
[26] T. Anticic et al. (NA49), Eur. Phys. J. **C65**, 9 (2010), arXiv:0904.2708 [hep-ex].
[27] H. G. Fischer (NA49), Quark and hadron dynamics, Acta Phys. Hung. **A17**, 369 (2003), Proceedings, Workshop, Budapest, Hungary, March 3-7, 2002.
[28] M. Aguilar et al. (AMS), Phys. Rev. Lett. **120**, 021101 (2018).
[29] M. Aguilar et al. (AMS), Phys. Rev. Lett. **119**, 251101 (2017).
[30] Q. Yan (AMS-02), "CR nuclei measurements with AMS-02: latest results and perspectives," (2017), XSCRC 2017, https://indico.cern.ch/event/563277/overview.
[31] J. J. Engelmann, P. Ferrando, A. Soutoul, P. Goret, and E. Juliusson, Astronomy and Astrophysics **233**, 96 (1990).
[32] N. Przybilla, M. F. Nieva, and K. Butler, Astrophys. J. **688**, L103 (2008), arXiv:0809.2403 [astro-ph].
[33] R. P. Duperray, C. Y. Huang, K. V. Protasov, and M. Buenerd, Phys. Rev. **D68**, 094017 (2003), arXiv:astro-ph/0305274 [astro-ph].
[34] A. Reinert and M. W. Winkler, (2017), arXiv:1712.00002 [astro-ph.HE].
[35] B. Baatar et al. (NA49), Eur. Phys. J. **C73**, 2364 (2013), arXiv:1207.6520 [hep-ex].
[36] D. Dekkers, J. A. Geibel, R. Mermod, G. Weber, T. R. Willitts, K. Winter, B. Jordan, M. Vivargent, N. M. King, and E. J. N. Wilson, Phys. Rev. **137**, B962 (1965).
[37] J. V. Allaby, F. G. Binon, A. N. Diddens, P. Duteil, A. Klovning, and R. Meunier, (1970), 10.17182/hep-data.1345.
[38] I. Arsene et al. (BRAHMS), Phys. Rev. Lett. **98**, 252001 (2007), arXiv:hep-ex/0701041 [hep-ex].
[39] F. Donato and P. D. Serpico, Phys.Rev. **D83**, 023014 (2011), arXiv:1010.5679 [astro-ph.HE].

Appendix A: Correlation matrices.

In Table VIII and Table IX we report the correlation matrices of the fits performed on the pp data with Param. I and II, respectively. Equivalently, Table X and Table XI contain the correlation matrices of the pA form factor Param. I-B and II-B.

Appendix B: Source term fraction in the future

The derivation of the source term in this paper reveals that the uncertainty of the cross sections to calculate the source term of CR antiprotons is still large compared uncertainties in the antiproton flux measured by AMS-02. This is partially due to the fact that the cross section coverage of the source term, namely, the fraction of the source term determined by the parameter space of cross section experiments is relatively small. In the context of Fig. 1 we discuss the situation of the pp channel. One very important step is to improve the coverage at low energies. NA61 has taken data of pp collisions at
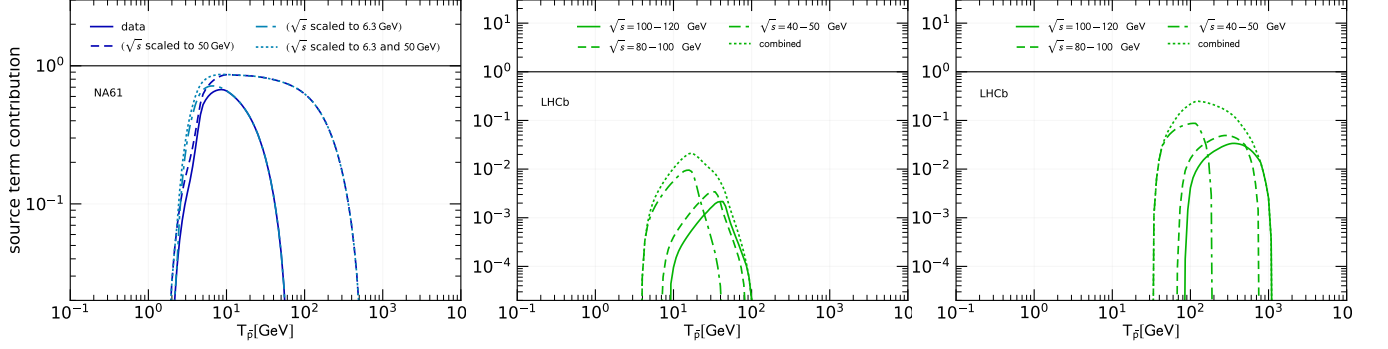
FIG. 10. Similar to Fig. 1 and Fig. 3. Fraction of the antiproton source term originating from the kinematic parameter space of the cross section which currently is experimentally determined by NA61 data in the pp channel (left panel) and by LHCb data in the pHe (central panel) or Hep (right panel) channels. We add future predictions for a possible evaluation of NA61 data at $\sqrt{s} = 6.3$ GeV and LHCb measurements at $\sqrt{s} = 43$ and 87 GeV. Each contribution is normalized to the total source term of the specific channel.
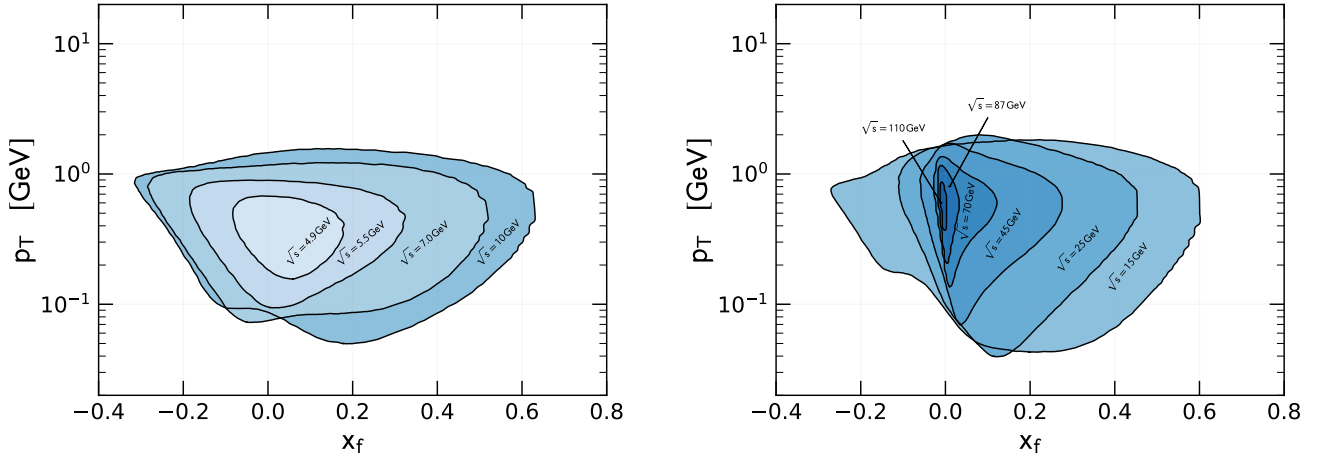

FIG. 11. Parameter space of the antiproton production cross section which is necessary to determine the antiproton source term at the uncertainty level of AMS-02 measurements [12]. We require the cross section to be known by 3% within the blue shaded regions and by 30% outside of the contours. The left and right panels contain contours for different CM energies. This figure is an update of Fig. 7b in DKD17. We exchange the kinetic variable x_{R} by x_f, which is suitable for the asymmetric pA cross section discussed in this paper.

$\sqrt{s} = 6.3$, 7.7, 8.8, 12.3, and 17.3 GeV, but evaluated $p + p \to \bar{p} + X$ only from $\sqrt{s} = 7.7$ GeV. In Fig. 10 (left panel) we show that the coverage of the source term could be improved down to $T_{\bar{p}} = 3$ GeV if NA61 would be able to analyze this data for antiprotons. We assume that the coverage in x_{R} and p_{T} is comparable to the measurement at $\sqrt{s} = 7.7$ GeV.

Similarly, one can guess further potentials in the pHe channels. The LHCb data are taken at very high energies of $\sqrt{s} = 110$ GeV and, therefore, their antiproton production in the energy range interesting for CRs results in a very small contribution to the source term, as shown in Fig. 3. We estimate the fraction of the $\bar{p}$ source term for measurements at $\sqrt{s} = 43$ and 87 GeV,

where we assume equal coverage in x_f and p_{T} as for the LHCb data at $\sqrt{s} = 110$ GeV. In Fig. 10 we show the source term fraction these measurements could achieve in the pHe (central panel) and Hep (right panel) channel. These measurements and especially their combination would significantly improve the coverage of the helium channels by LHCb.

Appendix C: Parameter space explorability

In DKD17 we studied the precision of cross section measurements which would be necessary to shrink the uncertainties imposed on the theoretical prediction of

the antiproton flux such that they are on the same level as flux measurement by AMS-02. We identified the relevant parameter space to be covered by high-energy particle physics experiments. We represented our results both in the LAB frame, where the target is at rest, and in the CM frame. Since we focused on proton-proton scattering and assumed a symmetric cross section, we presented our results for the CM system in terms of x_R. In this paper we discussed in detail the asymmetry in proton-nucleus scattering. The appropriate equivalent to x_R in this case is x_f. Therefore, here we update our main result from DKD17 and present the parameter space which should be covered by experiments in terms of x_f. The results presented in Fig. 11 are now applicable to any proton-nucleus production channel.

TABLE VIII. Correlation matrix of the pp fit with Param. I.

	C_1	C_2	C_3	C_4	C_5	C_6	C_7	C_8	ω_{BRAHMS}	ω_{Dekkers}	ω_{NA49}	ω_{NA61}
C_1	1.000	-0.994	0.000	-0.077	-0.002	-0.107	-0.019	0.131	-0.057	-0.226	0.100	0.117
C_2	-0.994	1.000	0.017	0.071	0.000	0.152	-0.015	-0.153	0.042	0.208	-0.082	-0.114
C_3	0.000	0.017	1.000	-0.847	-0.488	-0.217	0.288	0.452	-0.155	0.160	0.140	0.155
C_4	-0.077	0.071	-0.847	1.000	0.810	0.246	-0.355	-0.647	0.234	-0.022	0.007	-0.015
C_5	-0.002	0.000	-0.488	0.810	1.000	0.272	-0.450	-0.750	-0.026	0.088	0.011	0.051
C_6	-0.107	0.152	-0.217	0.246	0.272	1.000	-0.923	-0.422	-0.417	0.228	0.400	0.457
C_7	-0.019	-0.015	0.288	-0.355	-0.450	-0.923	1.000	0.532	0.541	-0.157	-0.131	-0.249
C_8	0.131	-0.153	0.452	-0.647	-0.750	-0.422	0.532	1.000	0.042	-0.039	-0.029	-0.058
ω_{BRAHMS}	-0.057	0.042	-0.155	0.234	-0.026	-0.417	0.541	0.042	1.000	-0.020	0.302	0.153
ω_{Dekkers}	-0.226	0.208	0.160	-0.022	0.088	0.228	-0.157	-0.039	-0.020	1.000	0.325	0.371
ω_{NA49}	0.100	-0.082	0.140	0.007	0.011	0.400	-0.131	-0.029	0.302	0.325	1.000	0.894
ω_{NA61}	0.117	-0.114	0.155	-0.015	0.051	0.457	-0.249	-0.058	0.153	0.371	0.894	1.000

TABLE IX. Correlation matrix of the pp fit with Param. II. Note that C_4 is a fixed parameter and therefore uncorrelated to the other parameters.

	C_1	C_2	C_3	C_4	C_5	C_6	ω_{Dekkers}	ω_{NA49}	ω_{NA61}
C_1	1.000	0.338	0.003	0.000	-0.214	0.055	0.057	0.951	0.843
C_2	0.338	1.000	0.312	0.000	0.207	0.355	0.035	0.075	-0.092
C_3	0.003	0.312	1.000	0.000	0.097	0.106	0.005	0.017	-0.019
C_4	0.000	0.000	0.000	1.000	0.000	0.000	0.000	0.000	0.000
C_5	-0.214	0.207	0.097	0.000	1.000	-0.127	0.666	-0.282	-0.289
C_6	0.055	0.355	0.106	0.000	-0.127	1.000	0.117	-0.043	-0.056
ω_{Dekkers}	0.057	0.035	0.005	0.000	0.666	0.117	1.000	0.050	0.065
ω_{NA49}	0.951	0.075	0.017	0.000	-0.282	-0.043	0.050	1.000	0.919
ω_{NA61}	0.843	-0.092	-0.019	0.000	-0.289	-0.056	0.065	0.919	1.000

TABLE X. Correlation matrix Param. I-B.

	D_1	D_2	ω_{LHCb}	ω_{NA49}
D_1	1.000	-0.516	0.603	0.798
D_2	-0.516	1.000	0.169	-0.008
ω_{LHCb}	0.603	0.169	1.000	0.745
ω_{NA49}	0.798	-0.008	0.745	1.000

TABLE XI. Correlation matrix Param. II-B.

	D_1	D_2	ω_{LHCb}	ω_{NA49}
D_1	1.000	-0.496	0.598	0.813
D_2	-0.496	1.000	0.216	-0.017
ω_{LHCb}	0.598	0.216	1.000	0.749
ω_{NA49}	0.813	-0.017	0.749	1.000